


# Modulation format identification in fiber communications using single dynamical node-based photonic reservoir computing

QIANG CAI,<sup>1,†</sup> YA GUO,<sup>1,2,†</sup> PU LI,<sup>1,3,4,\*</sup> ADONIS BOGRIS,<sup>5</sup>  K. ALAN SHORE,<sup>6</sup> YAMEI ZHANG,<sup>7</sup> AND YUNCAI WANG<sup>3</sup>

<sup>1</sup>Key Laboratory of Advanced Transducers and Intelligent Control System, Ministry of Education, Taiyuan University of Technology, Taiyuan 030024, China

<sup>2</sup>School of Electronics and Information, Northwestern Polytechnical University, Xi'an 710072, China

<sup>3</sup>School of Information Engineering, Guangdong University of Technology, Guangzhou 510006, China

<sup>4</sup>Key Laboratory of Specialty Fiber Optics and Optical Access Networks, Shanghai University, Shanghai 200444, China

<sup>5</sup>Department of Informatics and Computer Engineering, University of West Attica, Athens 12243, Greece

<sup>6</sup>School of Electronic Engineering, Bangor University, Wales LL57 1UT, UK

<sup>7</sup>Key Laboratory of Radar Imaging and Microwave Photonics, Ministry of Education, Nanjing University of Aeronautics and Astronautics, Nanjing 210016, China

\*Corresponding author: lipu8603@126.com

Received 9 September 2020; revised 12 November 2020; accepted 13 November 2020; posted 18 November 2020 (Doc. ID 409114); published 24 December 2020

We present a simple approach based on photonic reservoir computing (P-RC) for modulation format identification (MFI) in optical fiber communications. Here an optically injected semiconductor laser with self-delay feedback is trained with the representative features from the asynchronous amplitude histograms of modulation signals. Numerical simulations are conducted for three widely used modulation formats (on-off keying, differential phase-shift keying, and quadrature amplitude modulation) for various transmission situations where the optical signal-to-noise ratio varies from 12 to 26 dB, the chromatic dispersion varies from -500 to 500 ps/nm, and the differential group delay varies from 0 to 20 ps. Under these situations, final simulation results demonstrate that this technique can efficiently identify all those modulation formats with an accuracy of >95% after optimizing the control parameters of the P-RC layer such as the injection strength, feedback strength, bias current, and frequency detuning. The proposed technique utilizes very simple devices and thus offers a resource-efficient alternative approach to MFI. © 2020 Chinese Laser Press

<https://doi.org/10.1364/PRJ.409114>

## 1. INTRODUCTION

Fiber-optic communication systems are expected to be capable of adaptively adjusting various transmission parameters such as modulation formats, line rates, and spectrum assignments, based on the varying channel conditions and traffic demands in order to maximize the spectral and energy efficiencies [1–4]. The dynamic variation of transmission parameters imposes new requirements for the optical receivers in such elastic optical networks (EONs). To demodulate the transmission signal at the digital receivers, one must know the type of modulation format. Consequently, correct identification of modulation formats is rather crucial for high-quality communication [5,6].

The feature-based (FB) approach is an effective way to achieve modulation format identification (MFI) [7–11], carried out by using different tools to analyze the associated feature parameters from transmission signals. For instance, Nandi *et al.*

completed an identification of amplitude modulation (AM), frequency modulation (FM), M-ary amplitude shift-keying (MASK), and M-ary frequency-shift keying (MFSK) signals by analyzing their instantaneous phase and frequency information using the decision tree algorithm [9]. Park *et al.* realized the identification of MASK, MFSK, and M-ary phase-shift keying (MPSK) signals by employing the support vector machine to analyze the frequency features of modulated signals [10]. Khan *et al.* confirmed that using artificial neural network (ANN) can achieve the identification of six widely used modulation formats [including on-off keying (OOK), differential phase-shift keying (DPSK), M-ary quadrature amplitude modulation (MQAM), etc.] through analyzing their amplitude features [11].

Among them, ANN-based MFI technologies especially attract great attention due to their enormous calculation power and high accuracy. Typically, Wong *et al.* identified commonly

used MASK, MFSK, and MQAM signals using a multilayer perceptron (MLP) neural network [12]. O'Shea *et al.* successfully realized the identification of OOK, BPSK, MASK, MPSK, and MQAM signals by analyzing higher-order statistics with a convolutional neural network (CNN) [13]. Wang *et al.* implemented MFI on quadrature phase-shift keying (QPSK), phase-shift keying (PSK), and MQAM signals through a constellation diagram employing a deep neural network (DNN) with multiple nonlinear layers [14]. However, it should be pointed that a typical ANN architecture consists of at least three layers (i.e., the input layer, the hidden layer, and the output layer) with neuron nodes between two adjacent layers interlinked by variable trained weights.

Time-delayed reservoir computing (RC) [15] is a new type of ANN consisting of one nonlinear node under delayed feedback. For time-delayed RC, the nonlinear component under delayed feedback is used as the reservoir. Moreover, the output layer weight in the whole system is the only part that needs to be trained, and the process can be completed with low complexity.

Up to now, there have been many RCs reported based on optoelectronic or all-optical devices [16–30]. As far as we are aware of, the RC systems can complete complex computational tasks with high performance such as spoken digit recognition [17], nonlinear time series prediction [18], and wireless channel equalization [19]. In particular, photonic reservoir computing (P-RC) based on semiconductor lasers with time-delayed feedback is very promising for high-speed implementation of the RC. For instance, the P-RC performs the identification and classification of a packet header for switching in an optical network application [31,32]. In addition, the P-RC has been also proposed to address signal recovery in optical communication systems [33,34].

In this paper, the P-RC with semiconductor lasers is, for the first time to our knowledge, introduced to the field of MFI. After extracting representative features of amplitude histograms through asynchronous sampling OOK, differential quadrature phase-shift keying (DQPSK), and 16 quadrature amplitude modulation (16QAM) signals, we numerically implement correct identification results by means of the P-RC constructed with a delay-feedback semiconductor laser. Herein, we point

out that memory is a typical advantage of RC, especially compared to a feedforward NN. Memory in an RC originates from the recurrent network connections, allowing information to remain in the network over finite time. Past information therefore mixes with the current input. In our photonic RC, optical delayed feedback introduces recurrences resulting in the ring topology, so that the optical reservoir possesses this memory property. As the input of the reservoir in our task, the envelope of the asynchronous amplitude histogram from any modulation signal is almost continuous and shows a short-time relevance. Therefore, the memory in our RC needs to vanish after some time to allow responses to be influenced only by the recent past. This property is referred to as fading memory [35] and plays an important role in improving the identification performance.

Experiences demonstrate that the reservoir layer in the absence of input information should work in the nonlinear region to exhibit sufficiently different dynamical responses to input with different classes [20]. To accurately fix the corresponding nonlinear regime, we examine these critical hyperparameters (i.e., injection strength, feedback strength, response laser current, and frequency detuning) in a reasonable range based on the bifurcation diagram of the semiconductor lasers. Besides, based on our research on the nonlinear dynamics of semiconductor lasers [36,37], we find that the order of the hyperparameters does not matter. After that, we finally achieve an MFI with an overall estimation accuracy as high as 95%.

## 2. THEORETICAL MODEL

Figure 1 shows the schematic of the MFI based on the P-RC with semiconductor lasers. The whole system consists of three parts: input layer, reservoir, and output layer. In our implementation, the various modulation formats (OOK, DQPSK, QAM) commonly used in long-haul optical communication systems obtained their amplitude feature  $u(n)$  through asynchronous sampling. Specifically, the input  $u[n]$  is generated in the following way: 10 Gbps OOK, 40 Gbps DQPSK, and 100 Gbps 16QAM signals transmit over the emulated communication channel with different optical signal-to-noise

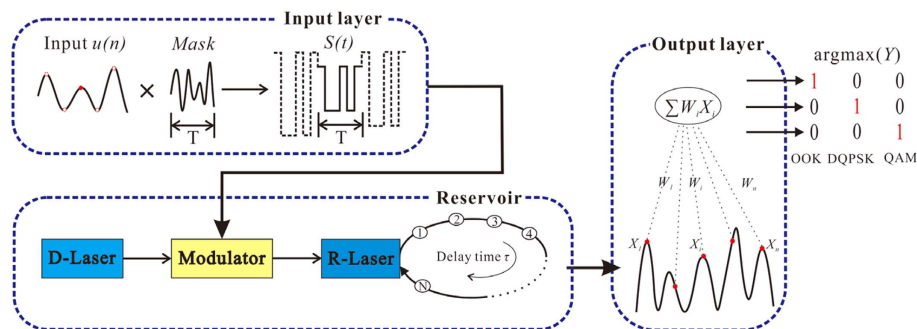


**Fig. 1.** Schematic of the MFI based on the P-RC with semiconductor lasers. This system consists of three parts: input layer, reservoir, and output layer. The input  $u(n)$  is multiplied by a mask with a period of  $T$ , and then the resulting stream  $S(t) = \text{Mask} \times u(n)$  is fed into the reservoir through a modulator. The reservoir is a master-slave configuration constructed by a response laser (R-Laser) with a self-delay feedback loop injected by a drive laser (D-Laser). Note that there are  $N$  virtual nodes at each interval  $\theta$  in the feedback loop with a delay time of  $T$ . The transient states of the R-Laser  $X_i$  are read out for training the connection weights  $W_i$  between the reservoir and the output layer. The final output nodes are weighted by the sums of the transient states  $\sum X_i W_i$ .

ratios (OSNRs)/chromatic dispersions (CDs)/differential group delays (DGDs) and are then asynchronously sampled at a sampling rate of 500 MSa/s in a duration time of 0.2 ms to obtain 100,000 amplitude samples. After normalizing all of the sampled amplitudes, we form the associated asynchronous amplitude histograms (AAHs) containing 100 bins as shown in the following Fig. 3. Finally, 11,700 sample data sets are generated and used as the input information  $u[n]$ . The input information is a one-dimensional data vector  $u(n)$ , where  $n \in Z$  is the discrete time. In the input layer,  $u[n]$  is preprocessed and multiplied by a mask sequence, which plays the role of random weight connections from the input to the reservoir layer. Note that different kinds of mask sequences can induce different effects on the RC performance. In the simulation, we actually investigated three kinds of commonly used mask signals, which are binary [38], six-level [39], and chaos masks [40], respectively. After analyzing their effect on the identification performance in the following Section 3, we finally select the chaos signal as the mask for RC. The amplitude feature  $u(n)$  first undergoes a sample-hold operation, where each sampling point has a duration of  $T$  and then is multiplied by a chaos mask sequence with a length of  $T$ . The resulting sequence  $S(t) = \text{Mask} \times u(n)$  is further injected into the following photonic reservoir.

In the reservoir, the optical signal from the drive laser (D-Laser) is modulated by the loaded signal  $S(t)$  from the input layer and then injected into the response laser (R-Laser) with a time-delayed optical feedback. Following ideas introduced in RC with the delay system, the input information generates nonlinear transient states in the context of previous input responses. This is because the induced transient states at time  $t$  depend on the output of the nonlinear node within the time interval  $[t - \tau, t]$ , with  $\tau$  being the delay time. In addition, the dynamics of the delay system exhibit the properties of high dimensionality and short-term memory, which accord well with the requirements of the P-RC. Within one delay interval of length  $\tau$ , the feedback delay loop contains  $N$  virtual nodes at each interval time  $\theta$  ( $\theta = \tau/N$ ). We denote these  $N$  equidistant points as “virtual nodes,” as their roles are actually analogous to the nodes of a traditional reservoir. The values of the delayed variable at each of the  $N$  points define the states of the virtual nodes, which show the transient response of the reservoir when the input information is at the specific time. The whole working process in the reservoir can be modeled by Eqs. (1) and (2) [30,40,41]:

$$\begin{aligned} \frac{dE(t)}{dt} = & \frac{1 + i\alpha}{2} \left\{ \frac{g[N(t) - N_0]}{1 + \varepsilon|E(t)|^2} - \frac{1}{\tau_p} \right\} E(t) \\ & + \frac{k_f}{\tau_{in}} E(t - \tau) \exp(-i2\pi\nu\tau) \\ & + \frac{k_{inj}}{\tau_{in}} E_{inj}(t) \exp(i2\pi\Delta\nu t) + \sqrt{2\beta N(t)} \chi(t), \quad (1) \end{aligned}$$

$$\frac{dN(t)}{dt} = J - \frac{N(t)}{\tau_s} - \frac{g[N(t) - N_0]}{1 + \varepsilon|E(t)|^2} |E(t)|^2, \quad (2)$$

where  $E$  is the slowly varying complex electric field and  $N$  is the average carrier density. The parameters  $k_f$  and  $k_{inj}$  represent the

feedback strength of external cavity of the R-Laser and the injection strength from the D-Laser to the R-Laser, respectively.  $\nu$  denotes the frequency of the free-running R-Laser, and  $\Delta\nu$  denotes the frequency detuning from the D-laser to the R-laser.  $J$  is the injection current. The carrier density at transparency  $N_0 = 4.55 \times 10^{23} \text{ m}^{-3}$ , the linewidth-enhancement factor  $\alpha = 5.0$ , the differential gain coefficient  $g = 1.414 \times 10^{-12} \text{ m}^3 \cdot \text{s}^{-1}$ , the gain saturation coefficient  $\varepsilon = 2.0 \times 10^{-23}$ , the internal cavity round-trip time  $\tau_{in} = 7.38 \text{ ps}$ , the photon lifetime  $\tau_p = 1.17 \text{ ps}$ , and the carrier lifetime  $\tau_s = 2.5 \text{ ns}$ , respectively. The feedback delay time  $\tau$  is 8 ns, and duration  $T = \tau \cdot \chi(t)$  is a white Gaussian noise with zero mean and unity variance, used to model the spontaneous emission noise.  $\beta$  is the strength of the spontaneous emission noise. [Note that the following simulation results are obtained at  $\beta = 0$ , except for the results in Table 3, where  $\beta = 1.5 \times 10^{-6}$ .] Considering that the input signal is multiplied with the mask being used to modulate the optical signal through phase modulation, the injected slowly varying complex electric field  $E_{inj}$  is written as Eq. (3):

$$E_{inj}(t) = \sqrt{I_d} \exp[i\pi S(t)], \quad (3)$$

where  $I_d$  is the photon number of continuous-wave output from the D-Laser,  $I_d = 3.757 \times 10^{20}$ .  $S(t)$  represents the masked input signal.

In the output layer, the transient states of the R-Laser  $X_i$  are read out for training the connection weights  $W_i$  between the reservoir and the output layer as defined in Eq. (4). Specifically, the optimal readout weights are calculated using the ridge regression algorithm in our work. The final output target  $Y(n)$  of three identified modulation formats is provided by using one-hot encoding [42] as follows. In the training stage of the P-RC, each input vector  $u(n)$  has a corresponding  $M \times 1$  binary vector  $Y$  with only one nonzero element. The location of ‘1’ in  $Y$  indicates the signal modulation format type:

$$Y(n) = \sum X_i W_i. \quad (4)$$

Once the training process of the P-RC is completed, we employ the error rate (ER) to evaluate the MFI performance by a separate set of data called testing data set as defined in Eq. (5). In the testing stage, the location of the largest element in each corresponding output vector  $v$ ,  $\text{argmax}\{v\}$ , is used as an identifier of the signal modulation format. The identified modulation formats are compared with true ones, which are provided by labels  $Y$  of the testing data set. Herein,  $Q$  represents the total of the samples of the testing data set, while  $b$  is the number of erroneous identification samples:

$$\text{ER} = \frac{b}{Q} \times 100\%. \quad (5)$$

### 3. NUMERICAL RESULTS AND DISCUSSIONS

As mentioned before, we choose 10 Gbps OOK, 40 Gbps DQPSK, and 100 Gbps 16QAM modulation format signals commonly used in long-haul fiber communication systems to validate the feasibility of our MFI proposal based on the P-RC in simulations. As shown in Fig. 2, these signals with three modulation formats transmit over a 30 km standard single-mode



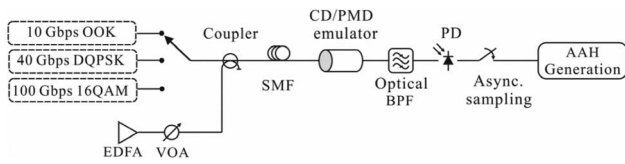


**Fig. 2.** Sketch of the emulated transmission system for asynchronous amplitude histogram generation. EDFA, erbium-doped fiber amplifier; SMF, single-mode fiber; CD/PMD, chromatic dispersion/polarization mode dispersion; BPF, band-pass filter; PD, photodetector; AAH, asynchronous amplitude histogram.

fiber (SMF; dispersion coefficient is  $16 \text{ ps}/(\text{nm} \cdot \text{km})$ , attenuation factor is  $0.2 \text{ dB}/\text{km}$ , and nonlinear coefficient is  $1.27 \text{ km}^{-1} \cdot \text{W}^{-1}$ ), respectively. An erbium-doped fiber amplifier (EDFA) is used to add amplified spontaneous emission (ASE) noise into the signals, while a variable optical attenuator (VOA) is used to adjust the OSNRs. A CD and a polarization mode dispersion (PMD) emulator are used to introduce variable amounts of CDs and DGDs into the signal, respectively. After removing the redundant noise by an optical band-pass filter (BPF) and direct detection by a photodetector (PD), the resulting electrical signal is asynchronously sampled to form asynchronous amplitude histograms (AAHs). The OSNR ranges considered in this work are the ones used in practice for reliable data transmission with the abovementioned signal types. There are various losses in the signal transmission process of optical fiber. Specifically, we investigate the three types of signals in the following scenarios: (i) their OSNRs are adjusted, ranging from 12 to 26 dB through a VOA at a step of 1 dB; (ii) their CDs are set, ranging from  $-500$  to  $500 \text{ ps}/\text{nm}$  via a CD emulator at a step of  $80 \text{ ps}/\text{nm}$ ; (iii) their DGDs are located by a PMD emulator in the range of  $0$ – $20 \text{ ps}$  with a step of  $5 \text{ ps}$ . Here we want to point out that using a fixed length of standard SMF with different OSNR and CD following is a common method to simulate the transmission system for asynchronous amplitude histogram generation [11,43]. In this way, the OSNR and CD can be easily adjusted to obtain associated data. Thus, we also apply this method in our simulation. Note that the nonlinear effects are very weak in the  $30 \text{ km}$  fiber propagation, and thus their impact is almost negligible.

Based on the above scenarios, 11,700 samples of modulation format signals in total are collected, and the randomly selected subsets of this large data set are then used for training and testing the performance of the P-RC. The examples of amplitude histograms for OOK, DQPSK, and 16QAM signals after asynchronous sampling are typically shown in Fig. 3. Herein, the OSNRs in each column are 12, 19, and 26 dB from left to right, but the corresponding CD and the DGD are fixed at  $80 \text{ ps}/\text{nm}$  and  $5 \text{ ps}$ , respectively. From each column, it can be clearly seen that different modulation formats exhibit distinct shapes. Even though the associated shapes change with various OSNRs from the first column to the third column, three types of modulation formats maintain distinct characteristics for each format. Therefore, the characteristic features of the asynchronous amplitude histograms have been widely accepted to be exploited for MFI.

In the following, we will use the features from the asynchronous amplitude histograms to train and test the P-RC so that

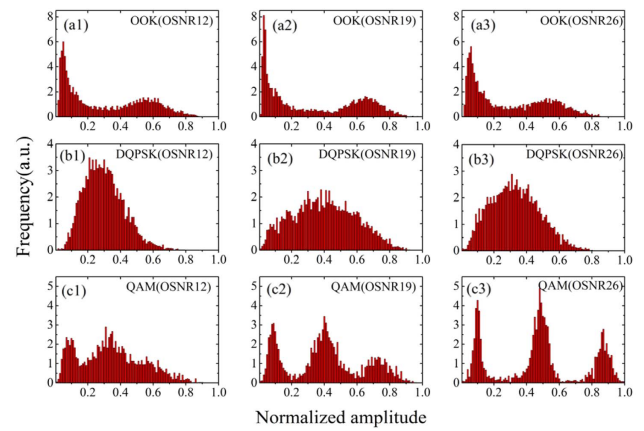


**Fig. 3.** Typical asynchronous amplitude histograms for (a1)–(a3) OOK, (b1)–(b3) DQPSK, and (c1)–(c3) QAM formats after propagation through the emulated communication channel. From left to right, each column has an OSNR of 12, 19, and 26 dB, while the corresponding CD and the DGD are fixed at  $80 \text{ ps}/\text{nm}$  and  $5 \text{ ps}$ , respectively.

MFI can be realized. At the first stage, we confirm the appropriate number of samples and the optimized size of the virtual nodes in the P-RC for high efficiency. In our scheme, we adopt the commonly used  $k$ -fold cross-validation algorithm [44] to eliminate the impact of the specific division of the available data samples between training and testing. This means that the entire process of training and testing is repeated  $k$  times (with  $k = 5$ ) on the same data, but each time with a different assignment of data samples to each of the two stages. The final ER in testing on the  $y$  axis is the mean across these  $k = 5$  runs. We compared the identification results with different types of mask signals (the binary mask, six-level mask, and chaos mask) by varying the sample numbers. The binary mask consists of a piecewise constant function with a randomly modulated binary sequence  $\{-1, 1\}$ . Similar to the binary mask, the six-level mask is composed of a random sequence  $\{\pm 1, \pm 0.6, \pm 0.3\}$ . The chaos mask signal is generated from another semiconductor laser with optical feedback [45]. Here the amplitude of the chaos mask is rescaled so that the standard deviation of the chaos mask is set to 1 and the mean value is set to 0. As shown in Fig. 4(a), the ER tends to be a stationary value when the sample number reaches around 2700. Meanwhile, it is clear that the chaos mask performs better than the other two types of masks. Thus, we select the chaos signal as the final mask in the following simulation. On the other hand, it can be observed that no matter whether the number of virtual nodes  $N$  in the P-RC is set as 300 or 400, the ER exhibits the same changing trend. Meanwhile, it should be noted that the ER corresponding to the virtual node number  $N = 400$  is lower than that in the other cases of  $N = 300$ .

As shown in Fig. 4(b), the ER decreases with the increase of the sample number and tends to be a stationary value. The red curve is the corresponding red curve (chaos mask) in Fig. 4(a). Consequently, 2700 samples of modulation signals and the virtual node number  $N = 400$  are selected in our simulation.

Furthermore, we analyze the effect of the four key parameters in the P-RC layer on the MFI performance, which are the

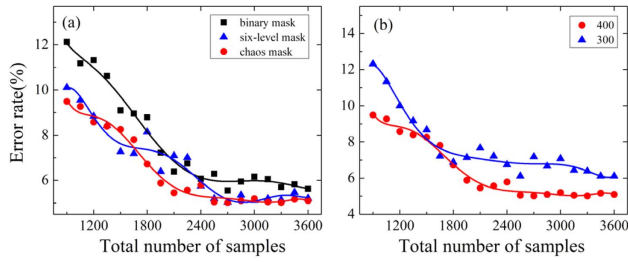


**Fig. 4.** (a) Identification error rate on the total (training and test) sample numbers of the binary mask (black), the six-level mask (blue), and the chaos mask signals (red). (b) Dependence of the identification error rate on the total (training and test) sample numbers at different virtual node sizes of 300 (blue) and 400 (red).

injection strength  $k_{inj}$  from the D-laser to R-laser, feedback strength  $k_f$  of the R-laser, bias current  $I_R$  of the R-laser, and frequency detuning  $\Delta\nu$  from the D-laser to R-laser. Figure 5 depicts the associated influence of the injection strength. When there is no input, the P-RC is a typical master-slave laser configuration. From its bifurcation diagram [Fig. 5(a)], one can observe that when the injection strength  $k_{inj}$  is less than 0.21, the output of the P-RC layer is in a chaotic state. With increase of the injection strength  $k_{inj}$ , the P-RC laser changes from the periodic oscillation state to a single-cycle state. On the other hand, Fig. 5(b) shows the dependence of the identification ER on the injection strength when the input is considered. It can be seen from Fig. 5(b) that the ER is first decreased but then increased with the increase of the injection strength  $k_{inj}$ . The lowest ER of 5.21% can be obtained when the optimum value of injection strength  $k_{inj}$  is equal to 0.2. Comparing its corresponding bifurcation diagram [Fig. 4(a)], it can be found that when  $k_{inj}$  is around 0.2, the delay-coupled semiconductor laser reservoir system in the absence of input works at the edge of the chaos region. This phenomenon is consistent with that in Ref. [15], where electrical reservoir computing based on a single dynamical node is used for standard benchmarking tasks such as spoken digit recognition and nonlinear time series prediction.

Figure 6 shows the effect of the feedback strength  $k_f$  of the R-laser on the identification performance. Here the injection strength  $k_{inj}$  is set at 0.2, while other parameters remain unchanged ( $I_R = 1.3I_{th}$  and  $\Delta\nu = -10$  GHz). When the feed-

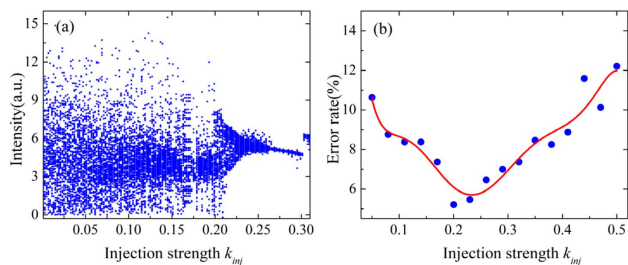


**Fig. 5.** (a) Bifurcation diagram of the output optical intensity versus the injection strength  $k_{inj}$  for  $k_f = 0.18$ ,  $I_R = 1.3I_{th}$ , and  $\Delta\nu = -10$  GHz. (b) Identification error rate (ER) at different injection strengths  $k_{inj}$  (blue dots), while the red curve is plotted by executing a sliding window averaging to the associated data points.

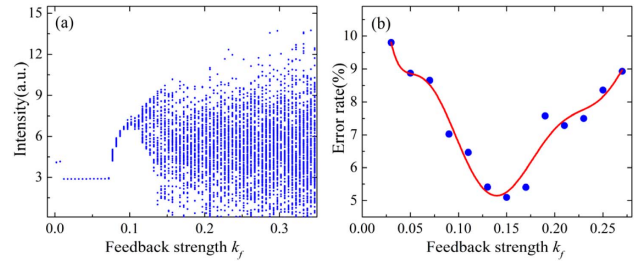
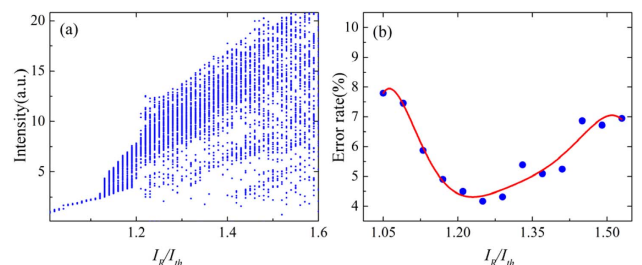


**Fig. 6.** (a) Bifurcation diagram of the output optical intensity versus the feedback strength  $k_f$  for  $k_{inj} = 0.2$ ,  $I_R = 1.3I_{th}$ , and  $\Delta\nu = -10$  GHz. (b) Identification ER at different feedback strengths  $k_f$  (blue dots), while the red curve is plotted by executing a sliding window averaging to the associated data points.

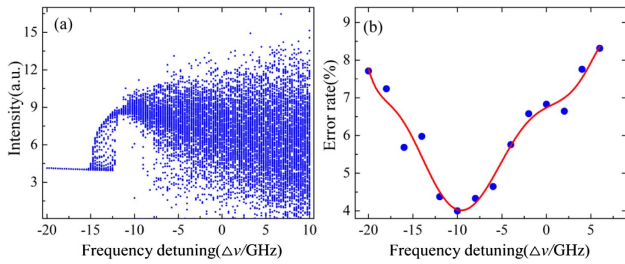
back strength  $k_f$  varies from 0.01 to 0.35, it can be seen from the corresponding bifurcation diagram in Fig. 6(a) that the output of the reservoir without the input follows a quasiperiodic route to chaos with the increase of the feedback strength  $k_f$ . After the input is considered, the final identification ER of our P-RC in Fig. 6(b) is decreased at first and then increased with increasing feedback strength  $k_f$ . When the feedback strength  $k_f$  is 0.15, the ER reaches a minimum value of 5.09%. When the feedback strength grows, the system is in the chaotic state and is more sensitive to changes in initial conditions. So the identification performance will decline.

Figure 7 illustrates the influence of the bias current  $I_R$  of the R-laser in the system. In the analysis, the injection strength  $k_{inj}$  and the feedback strength  $k_f$  are set to be 0.2 and 0.15, respectively. Figure 7(a) is the corresponding bifurcation diagram of the output optical intensity versus the bias current  $I_R$  of R-Laser. As can be seen, the RC subsystem will gradually leave a single-cycle state to the chaotic region when the bias current of the R-Laser increases from  $1.01I_{th}$  to  $1.6I_{th}$ . Note that  $I_{th}$  corresponds to the threshold current of the R-Laser. On the other hand, the identification ER in Fig. 7(b) first decreases and then increases with the increase of  $I_R$ . Finally, a minimum ER of 4.25% can be obtained when the bias current of the R-Laser equals  $1.25I_{th}$ .

Figure 8 investigates the influence of the frequency detuning  $\Delta\nu$  between the D-Laser and the R-Laser on the identification results. Figure 8(a) gives the bifurcation diagram as a function of the frequency detuning  $\Delta\nu$ . In the bifurcation diagram, the



**Fig. 7.** (a) Bifurcation diagram of the output optical intensity versus the bias current of the R-Laser  $I_R$  for  $k_{inj} = 0.2$ ,  $k_f = 0.15$ , and  $\Delta\nu = -10$  GHz. (b) Identification ER at different bias currents of the R-Laser  $I_R$  (blue dots), while the red curve is plotted by executing a sliding window averaging to the associated data points.



**Fig. 8.** (a) Bifurcation diagram of the output optical intensity versus the frequency detuning  $\Delta\nu$  between the D-Laser and the R-Laser for  $k_{inj} = 0.2$ ,  $k_f = 0.15$ , and  $I_R = 1.25I_{th}$ . (b) Identification ER at different frequency detunings  $\Delta\nu$  (blue dots), while the red curve is plotted by executing a sliding window averaging to the associated data points.

RC without the input can be observed in a single-cycle state when the frequency detuning  $\Delta\nu$  is  $-15$  GHz. With the increase of the frequency detuning  $\Delta\nu$ , it starts to enter a chaotic state at  $\Delta\nu = -10$  GHz. Figure 8(b) shows that the identification ER exhibits the same changing trend as Figs. 5(b), 6(b), and 7(b). That is, the ER decreases first and then increases with the increase of frequency detuning  $\Delta\nu$ . When the frequency detuning  $\Delta\nu$  is  $-10$  GHz, the ER can be reduced to a lowest value of 4.07%. Obviously, this best identification result is obtained at the edge of the chaos region by contrast with the bifurcation diagram. In this state, the RC has an infinite dimensional space so the input signal is mapped to the higher dimensional space and achieves the optimal identification results.

After the above processes, all key parameters in our P-RC can be adjusted to reach the optimum state as follows. (i) The number of virtual nodes  $N$  is chosen to be 400. (ii) The injection strength  $k_{inj}$  from the D-laser to the R-laser is set to be 0.2. (iii) The feedback strength  $k_f$  of the R-laser is set as 0.15. (iv) The bias current  $I_R$  of the R-Laser is  $1.25I_{th}$ . (v) The frequency detuning  $\Delta\nu$  between the D-Laser and R-Laser is set to  $-10$  GHz.

Under these conditions, we utilize the P-RC system to identify 1000 test cases with each type of modulation format for a considerable range of OSNRs (12–26 dB), CDs ( $-500$ – $500$  ps/nm), and DGDs (0–20 ps). Table 1 lists the associated test results of the proposed MFI technique through combining the ridge regression algorithm with the laser-based P-RC system. From it, one can confirm that the identification accuracies of OOK, DQPSK, and 16QAM sig-

**Table 1. Identification Accuracies for Different Modulation Formats Using the MFI Technique Through Our Laser-Based P-RC System<sup>a</sup>**

		Identified Modulation Formats		
		OOK	DQPSK	QAM
Actual Modulation Formats	OOK	95.1%	1.4%	1.7%
	DQPSK	3.2%	95.7%	2.8%
	QAM	1.7%	2.9%	95.5%

<sup>a</sup>The overall MFI accuracy is more than 95%.

nals can reach 95.1%, 95.7%, and 95.5%, respectively. These simulation results demonstrate that the proposed technique can effectively classify the modulation formats in fiber communication with an overall estimation accuracy of more than 95% and also in the presence of various link impairments such as OSNR, CD, and DGD. Meanwhile, in order to check the performance of our proposal, we also analyzed the MFI accuracy using only the ridge regression algorithm. In this case, the whole system only contains two layers: the input and output layers. The whole training process is as follows. The resulting sequence  $S$  from the input layer and the target matrix  $Y$  are directly used to calculate the final output connection weight  $W$  by means of the ridge regression algorithm. That is, there is no nonlinear mapping induced by the reservoir layer. The associated results on identification accuracies for different modulation formats are shown in Table 2. It is evident that the identification accuracies of all three modulation formats in the system only using the ridge regression algorithm are less than 76%. Therefore, we confirm that the identification accuracies can be significantly improved based on the proposed P-RC MFI system in our work.

Further, we investigate the influence of spontaneous emission noise on the performance of the P-RC. Table 3 shows the identification accuracies for different modulation formats using the MFI technique through the P-RC system under a typical spontaneous emission  $\beta = 1.5 \times 10^{-6}$  [46]. Comparing Table 1 and Table 3, one can find that our P-RC is extremely robust against spontaneous emission noise. That can be explained by the fact that the modulation format identification is a classification task that only requires a winner-takes-all decision. Note that the noise from the photodetector is additive, which can be eliminated using balance detection technology. Thus, the detection noise is not considered in this work.

**Table 2. Identification Accuracies for Different Modulation Formats Using Only the Ridge Regression Algorithm (Without the Reservoir Layer in the System)<sup>a</sup>**

		Identified Modulation Formats		
		OOK	DQPSK	QAM
Actual Modulation Formats	OOK	75.2%	8.2%	8.5%
	DQPSK	15.7%	72.6%	16.7%
	QAM	9.1%	19.2%	74.8%

<sup>a</sup>The overall MFI accuracy is less than 76%.

**Table 3. Identification Accuracies for Different Modulation Formats Using the MFI Technique Through the P-RC System with a Typical Noise Value of  $\beta = 1.5 \times 10^{-6}$ <sup>a</sup>**

		Identified Modulation Formats		
		OOK	DQPSK	QAM
Actual Modulation Formats	OOK	95.0%	1.2%	1.8%
	DQPSK	3.5%	95.5%	2.9%
	QAM	1.5%	3.3%	95.3%

<sup>a</sup>The overall MFI accuracy is more than 95%.



Finally, we want to point out that direct comparison with other works is difficult in modulation format identification as mentioned in Refs. [12,47]. There are two main reasons for this difficulty. (i) There is no single unified database available. When different modulation formats with different symbol rates are applied, different accuracies will result for NN-based modulation format identification. (ii) Identification accuracy is frequently reported as a function of OSNR and CD. There are no benchmarking systems universally agreed upon these indexes. For instance, Guesmi *et al.* reported an identification accuracy of 90% for 16 Gbps QPSK and 16QAM when the OSNR is 14–26 dB and the CD is 800 ps/nm [48]. Saif *et al.* showed an identification accuracy of 98% for 10 Gbps QPSK and 16QAM when OSNR is about 20 dB; however, when the symbol rate is enhanced into 20 Gbps, the associated identification accuracy is decreased to 90% [49]. Xiang *et al.* reported an identification accuracy of 100% for 28 Gbps QPSK and 16QAM when the CD is  $-60$ – $60$  ps/nm; but when the CD is in the other range, the identification accuracy is decreased below 90% [43].

There are at least two benefits to the P-RC. (i) High speed. Our P-RC is based on the all-optical nonlinearity of laser diodes. Such a system might even reach processing speeds at the level of 100 GHz using off-the-shelf photonic components for telecommunication applications [50]. (ii) Low energy consumption. At this stage we can only provide a conservative estimate, according to Ref. [16]. Our all-optical transient computing scheme, including all-optical data input and read-out hardware, would be of the order of 10 mJ per signal, compared with 2 J per signal required by a standard desktop computer.

In addition, the current accuracy level in this work is mainly constricted by the number of used nodes due to the limited sample size. Once the sample size is sufficiently large (that means more nodes are fully trained), there are two approaches to further achieve higher accuracy levels with P-RC. One is to improve the complexity of the mask [40]. In P-RC, the mask is equivalent to the input connection weight in the traditional RC. It can bring rich nonlinear states for P-RC and thus map the input data into a high-dimensional space. So it is expected that using a more complicated random signal (such as amplified spontaneous noise) as the mask may further enhance the identification accuracy. The other is to introduce the multiple feedback loops [30]. Usually, the P-RC system with multiple optical feedback results in a much more complex response of the R-laser compared to that with a single optical feedback. Consequently, higher dimensional transformation of the input signal and thus higher accuracy levels may be achieved with P-RC.

#### 4. CONCLUSION

In this paper, we propose a simple MFI technique for fiber-optic communications by using P-RC trained with amplitude features extracted from the OOK, DQPSK, and 16QAM signals through asynchronous sampling. Numerical results demonstrate over 95% identification accuracy for three widely used modulation formats in various situations under OSNRs (12–26 dB), CDs ( $-500$ – $500$  ps/nm), and DGDs

(0–20 ps). Considering the good performance and its conceptual simplicity, it can be expected that P-RC may provide an efficient tool for realizing the wide application of MFI in future fiber communication systems.

**Funding.** National Natural Science Foundation of China (61775158, 61961136002, 61927811, U19A2076, 61705159, 61805168, 17174343, 11904157); Program for Guangdong Introducing Innovative and Entrepreneurial Teams; Program for the Top Young Academic Leaders of High Learning Institutions of Shanxi; National Cryptography Development Fund (MMJJ20170127); China Postdoctoral Science Foundation (2018M630283, 2019T120197); Natural Science Foundation of Shanxi Province (201901D211116); STCSM (SKLSFO2018-03); Project of Key Laboratory of Radar Imaging and Microwave Photonics (Nanjing University of Aeronautics and Astronautics), Ministry of Education (RIMP2019002).

**Disclosures.** The authors declare no conflicts of interest.

<sup>†</sup>These authors contributed equally to this work.

#### REFERENCES

1. A. Nag, M. Tornatore, and B. Mukherjee, "Optical network design with mixed line rates and multiple modulation formats," *J. Lightwave Technol.* **28**, 466–475 (2010).
2. S. J. Yoo, A. Lord, M. Jinno, and O. Gerstel, "Elastic optical networking: a new dawn for the optical layer?" *IEEE Commun. Mag.* **50**, s12–s20 (2012).
3. T. Zhang, J. Wang, Q. Liu, J. Z. Zhou, J. Dai, X. Han, Y. Zhou, and K. Xu, "Efficient spectrum prediction and inverse design for plasmonic waveguide systems based on artificial neural networks," *Photon. Res.* **7**, 368–380 (2019).
4. Y. Q. Chang, H. Wu, C. Zhao, L. Shen, S. N. Fu, and M. Tang, "Distributed Brillouin frequency shift extraction via a convolutional neural network," *Photon. Res.* **8**, 690–697 (2020).
5. Z. Pan, C. Yu, and A. E. Willner, "Optical performance monitoring for the next generation optical communication networks," *Opt. Fiber Technol.* **16**, 20–45 (2010).
6. R. Borkowski, D. Zibar, and I. T. Monroy, "Anatomy of a digital coherent receiver," *IEICE Trans. Commun.* **E97-B**, 1528–1536 (2014).
7. E. E. Azzouz and A. K. Nandi, *Automatic Modulation Recognition of Communication Signals* (Kluwer Academic, 1996).
8. O. A. Dobre, A. Abdi, Y. Bar-Ness, and W. Su, "A survey of automatic modulation classification techniques: classical approaches and new trends," *IET Commun.* **1**, 137–156 (2007).
9. A. K. Nandi and E. E. Azzouz, "Algorithms for automatic modulation recognition of communication signals," *IEEE Trans. Commun.* **46**, 431–436 (1998).
10. C. S. Park, J. H. Choi, S. P. Nah, W. Jang, and D. Y. Kim, "Automatic modulation recognition of digital signals using wavelet features and SVM," in *10th International Conference on Advanced Communication Technology* (2008), pp. 387–390.
11. F. N. Khan, Y. Zhou, A. P. T. Lau, and C. Lu, "Modulation format identification in heterogeneous fiber-optic networks using artificial neural networks," *Opt. Express* **20**, 12422–12431 (2012).
12. M. L. D. Wong and A. K. Nandi, "Automatic digital modulation recognition using artificial neural network and genetic algorithm," *Signal Process.* **84**, 351–365 (2004).
13. T. J. O'shea, T. Roy, and T. C. Clancy, "Over the air deep learning based radio signal classification," *IEEE J. Sel. Top. Signal Process.* **12**, 168–179 (2018).

14. D. Wang, M. Zhang, J. Li, Z. Li, J. Li, C. Song, and X. Chen, "Intelligent constellation diagram analyzer using convolutional neural network-based deep learning," *Opt. Express* **25**, 17150–17166 (2017).
15. L. Appeltant, M. C. Soriano, G. Van der Sande, J. Danckaert, S. Massar, J. Dambre, B. Schrauwen, C. R. Mirasso, and I. Fischer, "Information processing using a single dynamical node as complex system," *Nat. Commun.* **2**, 468 (2011).
16. D. Brunner, M. C. Soriano, C. R. Mirasso, and I. Fischer, "Parallel photonic information processing at gigabyte per second data rates using transient states," *Nat. Commun.* **4**, 1364 (2013).
17. L. Larger, M. C. Soriano, D. Brunner, L. Appeltant, J. M. Gutierrez, L. Pesquera, C. R. Mirasso, and I. Fischer, "Photonic information processing beyond Turing: an optoelectronic implementation of reservoir computing," *Opt. Express* **20**, 3241–3249 (2012).
18. R. M. Nguimdo, G. Verschaffelt, J. Danckaert, and G. Van der Sande, "Fast photonic information processing using semiconductor lasers with delayed optical feedback: role of phase dynamics," *Opt. Express* **22**, 8672–8686 (2014).
19. L. Larger, A. Baylón-Fuentes, R. Martinenghi, V. S. Udaltsov, Y. K. Chembo, and M. Jacquot, "High-speed photonic reservoir computing using a time-delay-based architecture: million words per second classification," *Phys. Rev. X* **7**, 011015 (2017).
20. Y. Paquot, F. Duport, A. Smerieri, J. Dambre, B. Schrauwen, M. Haelterman, and S. Massar, "Optoelectronic reservoir computing," *Sci. Rep.* **2**, 287 (2012).
21. R. Martinenghi, S. Rybalko, M. Jacquot, Y. K. Chembo, and L. Larger, "Photonic nonlinear transient computing with multiple-delay wavelength dynamics," *Phys. Rev. Lett.* **108**, 244101 (2012).
22. F. Duport, B. Schneider, A. Smerieri, M. Haelterman, and S. Massar, "All-optical reservoir computing," *Opt. Express* **20**, 22783–22795 (2012).
23. K. Hicke, M. A. Escalona-Morán, D. Brunner, M. C. Soriano, I. Fischer, and C. R. Mirasso, "Information processing using transient dynamics of semiconductor lasers subject to delayed feedback," *IEEE J. Sel. Top. Quantum Electron.* **19**, 1501610 (2013).
24. A. Dejonckheere, F. Duport, A. Smerieri, L. Fang, J. L. Oudar, M. Haelterman, and S. Massar, "All-optical reservoir computer based on saturation of absorption," *Opt. Express* **22**, 10868–10881 (2014).
25. R. M. Nguimdo, G. Verschaffelt, J. Danckaert, and G. Van der Sande, "Simultaneous computation of two independent tasks using reservoir computing based on a single photonic nonlinear node with optical feedback," *IEEE Trans. Neural Netw. Learn. Syst.* **26**, 3301–3307 (2015).
26. Q. Vinckier, F. Duport, A. Smerieri, K. Vandoorne, P. Bienstman, M. Haelterman, and S. Massar, "High performance photonic reservoir computer based on a coherently driven passive cavity," *Optica* **2**, 438–446 (2015).
27. J. Bueno, D. Brunner, M. C. Soriano, and I. Fischer, "Conditions for reservoir computing performance using semiconductor lasers with delayed optical feedback," *Opt. Express* **25**, 2401–2412 (2017).
28. J. Vatin, D. Rontani, and M. Sciamanna, "Experimental reservoir computing using VCSEL polarization dynamics," *Opt. Express* **27**, 18579–18584 (2019).
29. X. Tan, Y. Hou, Z. Wu, and G. Xia, "Parallel information processing by a reservoir computing system based on a VCSEL subject to double optical feedback and optical injection," *Opt. Express* **27**, 26070–26079 (2019).
30. Y. Hou, G. Xia, W. Yang, D. Wang, E. Jayaprasath, Z. Jiang, C. Hu, and Z. Wu, "Prediction performance of reservoir computing system based on a semiconductor laser subject to double optical feedback and optical injection," *Opt. Express* **26**, 10211–10219 (2018).
31. J. Qin, Q. Zhao, D. Xu, H. Yin, Y. Chang, and D. Huang, "Optical packet header identification utilizing an all-optical feedback chaotic reservoir computing," *Mod. Phys. Lett. B* **30**, 1650199 (2016).
32. J. Qin, Q. Zhao, H. Yin, Y. Jin, and C. Liu, "Numerical simulation and experiment on optical packet header recognition utilizing reservoir computing based on optoelectronic feedback," *IEEE Photon. J.* **9**, 7901311 (2017).
33. A. Argyris, J. Bueno, and I. Fischer, "Photonic machine learning implementation for signal recovery in optical communications," *Sci. Rep.* **8**, 8487 (2018).
34. A. Argyris, J. Bueno, and I. Fischer, "PAM-4 transmission at 1550 nm using photonic reservoir computing post-processing," *IEEE Access* **7**, 37017–37025 (2019).
35. H. Jaeger, "Short term memory in echo state networks," *GMD Rep.* **152**, 60 (2002).
36. A. Wang, Y. Wang, and H. He, "Enhancing the bandwidth of the optical chaotic signal generated by a semiconductor laser with optical feedback," *IEEE Photon. Technol. Lett.* **20**, 1633–1635 (2008).
37. A. Wang, Y. Wang, and J. Wang, "Route to broadband chaos in a chaotic laser diode subject to optical injection," *Opt. Lett.* **34**, 1144–1146 (2009).
38. L. Appeltant, G. Van der Sande, J. Danckaert, and I. Fischer, "Constructing optimized binary masks for reservoir computing with delay systems," *Sci. Rep.* **4**, 3629 (2015).
39. M. C. Soriano, S. Ortín, D. Brunner, L. Larger, C. R. Mirasso, I. Fischer, and L. Pesquera, "Optoelectronic reservoir computing: tackling noise-induced performance degradation," *Opt. Express* **21**, 12–20 (2013).
40. J. Nakayama, K. Kanno, and A. Uchida, "Laser dynamical reservoir computing with consistency: an approach of a chaos mask signal," *Opt. Express* **24**, 8679–8692 (2016).
41. R. Lang and K. Kobayashi, "External optical feedback effects on semiconductor injection laser properties," *IEEE J. Quantum Electron.* **16**, 347–355 (1980).
42. S. Okada, M. Ohzeki, and S. Taguchi, "Efficient partition of integer optimization problems with one-hot encoding," *Sci. Rep.* **9**, 13036 (2019).
43. Q. Xiang, Y. Yang, Q. Zhang, and Y. Yao, "Joint and accurate OSNR estimation and modulation format identification scheme using the feature-based ANN," *IEEE Photon. J.* **11**, 7204211 (2019).
44. Y. Bengio and Y. Grandvalet, "No unbiased estimator of the variance of K-fold cross-validation," *J. Mach. Learn. Res.* **5**, 1089–1105 (2004).
45. P. Li, Q. Cai, J. Zhang, B. Xu, Y. Liu, A. Bogris, K. A. Shore, and Y. Wang, "Observation of flat chaos generation using an optical feedback multi-mode laser with a band-pass filter," *Opt. Express* **27**, 17859–17867 (2019).
46. A. Zhao, N. Jiang, C. Xue, J. Tang, and K. Qiu, "Wideband complex-enhanced chaos generation using a semiconductor laser subject to delay-interfered self-phase-modulated feedback," *Opt. Express* **27**, 12336–12348 (2019).
47. B. G. Mobasser, "Digital modulation classification using constellation shape," *Signal Process.* **80**, 251–277 (2000).
48. L. Guesmi, A. M. Ragheb, H. Fathallah, and M. Menif, "Experimental demonstration of simultaneous modulation format/symbol rate identification and optical performance monitoring for coherent optical systems," *J. Lightwave Technol.* **36**, 2230–2239 (2017).
49. W. S. Saif, A. M. Ragheb, H. E. Seleem, T. A. Alshawi, and S. A. Alshebeili, "Modulation format identification in mode division multiplexed optical networks," *IEEE Access* **7**, 156207 (2019).
50. I. Park, I. Fischer, and W. Elsässer, "Highly nondegenerate four-wave mixing in a tunable dual-mode semiconductor laser," *Appl. Phys. Lett.* **84**, 5189–5191 (2004).